Book Chapter

Film-Forming Kinetics in Organic Solar Cells

Qiuju Liang[1] and Jiangang Liu[2]*

[1]School of Microelectronics, Northwestern Polytechnical University, China
[2]School of Electronics and Information, Northwestern Polytechnical University, China

***Corresponding Author:** Jiangang Liu, School of Electronics and Information, Northwestern Polytechnical University, Xi'an 710129, China

Published **March 04, 2022**

This Book Chapter is a republication of an article published by Jiangang Liu, et al. at Energies in November 2021. (Liang, Q.; Yao, J.; Hu, Z.; Wei, P.; Lu, H.; Yin, Y.; Wang, K.; Liu, J. Recent Advances of Film–Forming Kinetics in Organic Solar Cells. Energies 2021, 14, 7604. https://doi.org/10.3390/en14227604)

How to cite this book chapter: Qiuju Liang, Jiangang Liu. Film-Forming Kinetics in Organic Solar Cells. In: Maria Portarapillo and Ahmad Karnama, editors. Advances in Energy Research: 3rd Edition. Hyderabad, India: Vide Leaf. 2022.

Acknowledgments: This work was supported by the National Natural Science Foundation of China (51773203, 51903211, 52073231), the Fundamental Research Funds for the Central

Universities (D5000200273, D5000210689), the China Postdoctoral Science Foundation (2020T130535, 2020M673468) and the National Aerospace Science Foundation of China (2020Z073053010).

Abstract

Solution-processed organic solar cells (OSC) have been explored widely due to their low-cost and convenience and impressive power conversion efficiencies (PCEs) have surpassed 18%.In particular, the optimization of film morphology including the phase separation structure and crystallinity degree of donor and acceptor are crucially important to the improvement of PCE. Considering that the film morphology optimization of many blends can be achieved by regulating the film-forming process, it is necessary to take more note to the employment of solvents and additives used during film processing, as well as the film-forming conditions. Herein, we summarize the recent investigations about thin-film and expect to give some guidance for its prospective progress. The different film morphologies are discussed in detail to expound the relationship between the morphology and devices performance. Then, the principle of morphology regulating is concluded. Finally, a future controlling of the film morphology and development is briefly outlooked, which may provide some guidance for further optimizing the device performance.

Keywords

Organic Solar Cells; Solution Process; Morphology; Film-Forming Kinetics

Introduction

Organic solar cells (OSCs) have been recognized as one of the most promising green devices to convert solar energy to electricity, which possesses the advantages of lightweight, flexibility, printing processable and large-area production [1-4]. OSCs consist of anode, cathode and active layer between them. By 2021, thanks to the favorable development of donor and

acceptor materials, optimization of active layer morphology and maturity of processing technology, the OSCs have realized outstanding power conversion efficiency (PCE) over 18% for binary devices [5-12]. These devices based on ternary active layer can achieve the same or better performance [13-19].

The performance of OSCs devices is closely related to the morphology of the active layer, because it crucially affects photophysical conversion process. The photophysical conversion process usually includes photon absorption (exciton generation), exciton diffusion, exciton separation, carrier transport and collection [20]. After the active layer absorbed a photon, the electron in donor's highest occupied molecular orbital (HOMO) is excited and jumps to the donor's lowest unoccupied molecular orbital (LUMO) to form a electron-hole pair bounded by coulomb forces. Because of the strong binding energy (0.35 ~ 0.5 eV), the exciton cannot be separated through thermal vibration [21,22]. Therefore, the exciton separation can only rely on the electric field gravity provided by the built-in electric field at the donor/acceptor (D/A) interfaces. However, if the domain size is too large, some excitons cannot reach the D/A interfaces due to their short lifetime [23,24]. Only the excitons near the D/A interface (5~10 nm) can reach the interfaces and get the chance to dissociate into electrons and holes driven by the built-in electric field. Therefore, the appreciate domain size is usually 10 ~ 20 nm in OSCs [25,26]. According to previous researches, the molecular orientation of donor and acceptor at interface directly determines the driving forces of the built-in electric field [27]. When the orientation of donor and acceptor is consistent, the coupling force between the donor and acceptor is large, leading to a strong built-in electric field, which is benefit for exciton dissociation [28-30]. Furthermore, generated free electrons and holes need to transport to the corresponding anode and cathode through the pure acceptor and donor phases, respectively. Hence, the bi-continuous separated donor and acceptor phases, i.e., an interpenetrating network structure is highly desirable for carrier transmission [31-35]. In addition, high carrier mobility ensures the efficiency of charge collection, hence high crystallinity degree of donor and acceptor is required because it reduces the energy barrier of charge transport and

helps obtaining high carrier mobility. [36-41]. Also, the donor and acceptor should enrich at anode and cathode, respectively, which can effectively reduce the bimolecular recombination, thereby improving the charge collection [42]. According to the relationship between morphology of active layer and photoelectric process of devices, it is obvious that the active layer should possess a highly crystalline interpenetrating network with proper domain size and face-on molecular orientation.

Therefore, on the basis of molecular tailoring [43, 44], researchers have invented a variety of methods for optimizing the morphology of the active layer. One of most widely used effective methods is thermal annealing (TA), which can enhance molecular stack and degree of crystallinity of donor and acceptor. [45-49]. For example, in P3HT:SF-HR blends thin films, the diffraction intensity becomes much clearer, which means the degree of crystallinity of both donor and acceptor increases dramatically after TA at 120 ℃[50]. Similar to TA, solvent vapor annealing (SVA) is also an effective method to optimize the film morphology. [51-55]. Hou et al. used dichloromethane SVA treated DRTB-T:IC-C6IDT-IC-based blend film for 60 s, and the ordered aggregation of donor and acceptor is promoted, which facilitate the formation of interpenetrating network structure. This optimized phase separation structure is conducive to the exciton dissociation and carrier transport, boosting the PCE of the device from 5.03% to 9.08% [56]. However, it is a challenge to combine the two methods to practical large area manufacture because TA is difficultly to employ to treat the flexible substrates of low glass transition temperature, and SVA is not compatible with roll-to-roll processes [57,58].

Furthermore, the morphology of the BHJ active layer closely depends on the film-forming process of solution processing [59,60]. During the evaporation of solvent, the solution layer gradually evolves from liquid state to solid state on the substrate, and the formed film is frozen in thermodynamic metastable state. The film-forming process decides the film quenching depth of the frozen state. For example, through extending the

film-forming time, the donor and acceptor molecules have sufficient time to diffuse and rearrange leading to enhanced crystallinity of the film and increased domain sizes. If the donor and acceptor are precipitated simultaneously in short time during the film-forming process, the degree of crystallinity of both donor and acceptor is low since the insufficient self-aggregating time. Therefore, controlling the kinetic process of film-forming process can also regulate the morphology of active layer.

This review focuses on the influence of the film-forming kinetics process on the morphology of the active layer in OSCs and the underlying mechanisms are revealed. Furthermore, methods used to regulate the film-forming kinetics process are summarized and representative examples are given and discussed to understand the key parameters on tuning film-forming process. Finally, a future controlling and development of film-forming kinetics is briefly outlooked, which may give some guidance to achieve high PCE of OSCs.

The Effect of the Film-Forming Kinetics on Film Morphology

The Film-Forming Kinetics Affect the Degree of Crystallinity of the Blend Film

Due to the semicrystalline character of the conjugated molecules, the crystalline phase and amorphous phase always coexist in the active layer. For crystalline phase, the degree of intermolecular coupling is high, which reduces the energy barrier of carrier transport and is benefit for carrier mobility. For the amorphous phases, the large energy barrier is adverse to carrier transport. However, if the duration of film-forming process is too short, the time for molecules in the solution to diffuse and self-organize is insufficient. Consequently, most molecules tend to be frozen in amorphous state, which leads to a low degree of crystallinity. Therefore, extending the film-forming duration is an effective strategy to improve the crystallinity.

Adding additive or using solvent with high boiling point (b.p.) can prolong the film-forming process effectively. Professor

DeLongchamp group investigated the effect of additives, 1,8-octanedithiol (ODT, b.p. ≈ 270 °C) and 1-chloronaphthalene (CN, b.p. ≈ 263 °C), on the film-forming process of poly (3-hexylthiophene)/phenyl-C61-butyric acid methyl ester (P3HT/PCBM) blend solution, and the main solvent is chlorobenzene (CB, b.p. ≈ 131 °C) [61]. From the extinction coefficient ratio and the evolution of film thickness (Figure1c, d, f, g), it is clear that the film-forming duration was prolonged from ca. 20 s to 30 s and even110 s, respectively. The extended film-forming process provide enough time for self-aggregation of both P3HT and PCBM. As a result, the relative the crystal diffraction value of the film with 2% ODT and CN increased from the initial 0.6 to more than 0.8. The improved degree of crystallinity facilitates carrier transport, and hole mobility and charge extraction can be impacted positively through the additive processing [62, 63]. Take the addition of ODT for instance, the addition of additive increased the J_{sc} from 1.67 mA/cm^2 to 8.87 mA/cm^2, boosting the PCE from 0.58% to 3.13%.

Not only the crystallinity of P3HT/PCBM film was improved after adding ODT or CN, the crystal size was enlarged as well. Energy-filtered transport electron microscope (EFTEM) was employed to characterize the variation of crystal size. As shown in Figure 2b-d, the crystal size of P3HT is just a few nanometers in both wide and long direction. While after the addition of additive, the width of P3HT fibers increased to 20 ~ 30 nm, and its length is approximately several hundred nanometers. Meanwhile, tiny nodule structures of PCBM phases also exist among P3HT nanofibers, which guarantee the exciton dissociation. This phenomenon can be explained in the view of ratioof characteristic length scale (R) and exciton diffusion length (RS), which has positive correlation with the crystallinity and phase purity. The group characterized the Rs using in-situ fluorescence spectroscopy (PL spectroscopy) [64]. The results showed that the R/RS increased to ~ 0.7 and ~ 0.95 after the addition of additive due to the increased phase purity and crystallinity [65]. Consequently, the highest exciton dissociation efficiency (about 94%) and high internal quantum efficiency (IQE) could be obtained from the device processed with adding 2% CN [66].

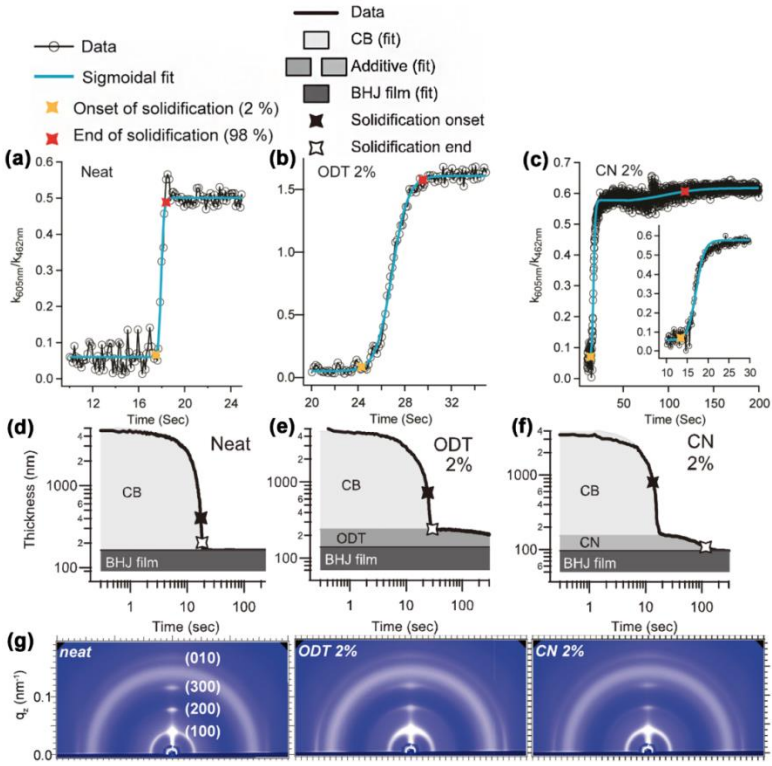

Figure 1: The film-forming process of P3HT/PCBM blend from CB solution (a)(d) without additives, (b)(e) with 2% ODT and (c)(f) with 2% CN. (a-c) The evolution of the extinction coefficient (k) at 605 nm to k at 462 nm. (d-f) Film thickness evolution. (g) GIWAXS diffraction patterns of different solid films [61].

To further reveal the underlying mechanism of the formation of solid films under different solvent systems, in-situ grazing incidence wide-angle X-ray scatting (GIWAXS), in-situ spectroscopic ellipsometry (SE) and film thickness test were employed to study the film-forming kinetics [67]. As shown in Figure 3, without any additives, the main solvent CB evaporates quickly and the time of film-forming is very short. This fast film-forming process cannot provide sufficient time for the donor and acceptor to aggregate and crystallize, which resulting in both donor and acceptor frozen amorphous state. When CN was added, after CB was fully evaporated, P3HT crystal and CN

solution of donor and acceptor remained in the film. And P3HT can aggregate at a lower degree of supersaturation in CN and ODT, hence, P3HT continues to crystalline during CN and ODT evaporating. Furthermore, the CN and ODT can selectively dissolve PCBM inferred from Table 1, and after the crystallization of P3HT, the PCBM can diffuse out from the P3HT domains. Furthermore, the ODT avoids too excessive crystallization of donor, which makes the crystallinity more balanced.

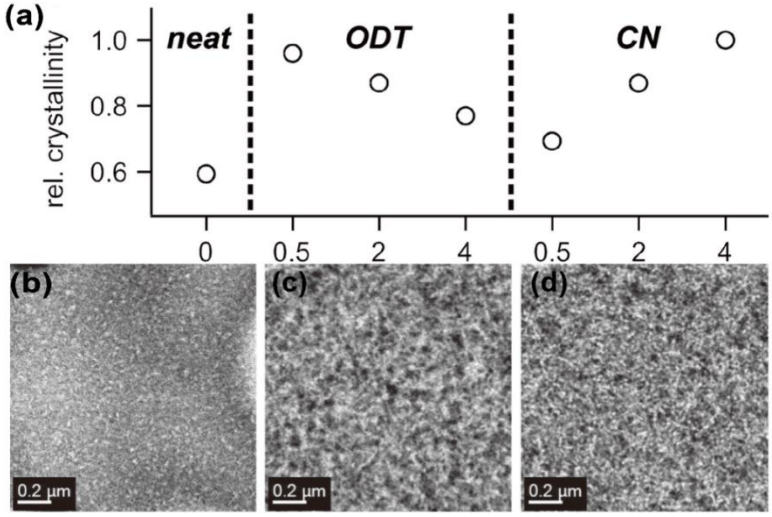

Figure 2: (a) The final relative crystallinity of P3HT/PCBM blend BHJ film from CB solution without additives and with additive in different concentration. TEM images of films processed (a) with no additive, (b) with 2% ODT, and (c) with 2% CN. P3HT domain is bright, PCBM domain is dark [61].

Table 1: Solubility of P3HT、PCBM in CB、CN、ODT.

Solvent		Solubility (mg/mL)	
		P3HT	PCBM
Chlorobenzene (CB)		14	35
Additives	1,8-octanedithiol (ODT)	0.50	30
	1-chloronaphthalene (CN)	6.4	37

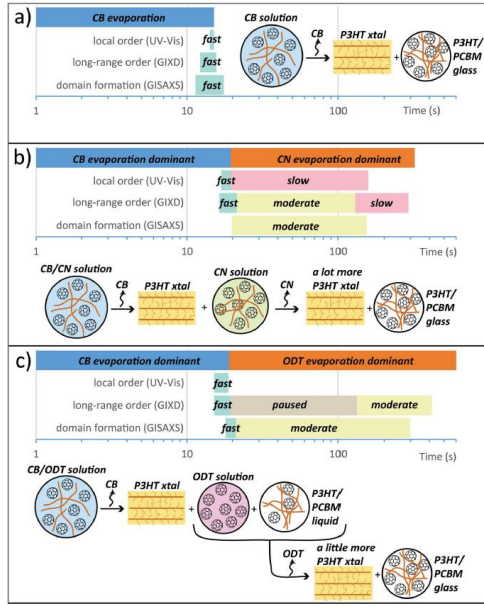

Figure 3: Schematic image of film drying process in different solvent systems [67].

Besides the typical polymer/PCBM blends, extending the film-forming process could also improve the crystallinity of all-small molecular blends and all-polymer blends. McDowell C. et al. studied the different influence of CB/polystyrene (PS) binary solvent and CB/PS/1,8–diiodooctane (DIO, b.p. ≈ 168 °C) ternary solvent on the film-forming process of the 7,7'-(4,4-bis(2-ethylhexyl)-4H-silolo[3,2-b:4,5-b']dithiophene-2,6-diyl)bis(6-fluoro-4-(5'-hexyl-[2,2'-bithiophen]-5yl)-benzo[c][1,2,5]thiadiazole (*p*-DTS(FBTTh$_2$)$_2$) /[6,6]-phenyl C71-butyric acid methyl ester (PC$_{71}$BM) blends [68]. The film-forming duration increased from 46 s to > 1800 s after the addition of DIO (Figure 4a). In Figure 4b, the diffraction peaks at 4.4 nm-1 (yellow region) originated from the metastable state, and the one centered at 2.8 nm-1 (green region) is corresponding to *p*-DTS(FBTTh$_2$)$_2$ alkyl chain stacking in crystals. The metastable GIWAXS diffraction peaks at 4.4 nm-1 disappeared, while the diffraction peaks of *p*-DTS(FBTTh$_2$)$_2$ alkyl chain around 2.8 nm-1 were significantly enhanced. The result indicated enhanced degree of crystallinity which was mainly attributed to the sufficient time for sufficient migration and

rearrangement during the prolonged film-forming process rather than freezing at metastable state in the short film-forming process. The enhanced crystallinity of *p*-DTS(FBTTh$_2$)$_2$ was also confirmed in this article as shown in Figure 4d. Comparing with the morphology of film processed with CB/PS in Figure 4c, many crystalline fibrils of *p*-DTS(FBTTh$_2$)$_2$ can be observed interspersing the PS phases in the film processed with CB/PS/DIO (Figure 4d), which implies more *p*-DTS(FBTTh$_2$)$_2$ self-organize into crystals in the extended film-forming process.

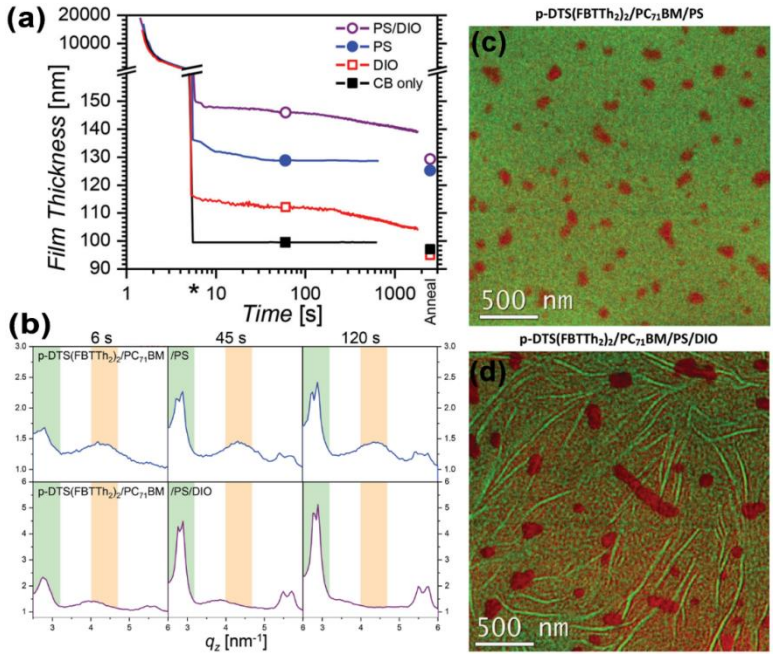

Figure 4: (a) The thickness evolution of p-DTS(FBTTh2)2/PC$_{71}$BM blend film in main solvent CB without additive (black), with PS additive (blue), with DIO additive (red) and with PS and DIO additive (purple). (b) The GIWAXS diffraction intensity of *p*-DTS(FBTTh$_2$)$_2$/PC$_{71}$BM/PS/CB and *p*-DTS(FBTTh$_2$)$_2$/PC$_{71}$BM/PS/DIO/CB blends at 6s、45s、120s during film-forming process. (c) EFTEM image of the dry film from p-DTS(FBTTh2)2/PC$_{71}$BM/PS/CB solution and (d) p-DTS(FBTTh2)2/PC$_{71}$BM/PS/DIO/CB solution, green regions and red regions are *p*-DTS(FBTTh$_2$)$_2$ rich phases and PC$_{71}$BM and PS rich phases, respectively [68].

In some highly crystalline blend systems, the crystallization would induce phase separation, leading to too large domain size.

Shortening the film-forming process is an efficient way to decrease the domain size, because it could freeze more molecules in amorphous state, which reduce the driving force of phase separation. Employing the solvent with low b.p. as main solvent is one of effective methods to shorten the film-forming duration. Zhu et al. used 2-methyltetrahydrofuran (MTHF, b.p.=80 °C) to replace CB (b.p.=132 °C) to accelerate solvent evaporation process of the poly{(4,8-bis(5-(2-ethylhexyl)thiophen-2-yl)benzo[1,2-b:4,5-b']dithiophene-co-4,8-di(thien2-yl)-2-(6-(1,1,1,3,5,5,5-heptamethyltrisiloxan-3-yl)hexyl)-6octyl[1,2,3]triazolo[4,5-f]isoindole-5,7(2H,6H)-dione} (PTzBI-Si) /poly{[N,N-9-bis(2-octyldodecyl)-naphthalene-1,4,5,8-bis(dicarboximide)-2,6-diyl]-alt-5,50-(2,20-bithiophene)} (N2200) blends, and the film-forming time is shortened from ~11.7 s in CB to ~3.7 s in MTHF (See Figure 5b) [69]. The shortened film-forming duration caused the decreased crystallinity, which suppressed the formation of large-scale phases. Meanwhile, it also reduced the diameter of fibrous PTzBI-Si crystals from larger than 400 nm to 35 nm (Figure 5a). The optimized morphology facilitated the exciton dissociation, boosting the J_{sc} from 2.76 mA cm^{-2} to 15.41 mA cm^{-2}, which leads to the PCE increased from 1.01% to 9.01%.

In addition to solvent engineering, elevating the temperature of substrate could also shorten the film-forming process as well. Wang et al. shortened the film-forming process of PBDB-T/INPIC-4F (the molecular structure and energy level are shown in Figure 6a and b for) blends to reduce the domain size through elevating the substrate temperature from room temperature (RT) to 100 °C [70]. INPIC-4F preferred to grow into large polycrystalline spherulites when casted on the substrate under room temperature with solvent-vapor (SV) atmosphere due to long self-organizing time, leading to a low PCE value of 9.9% (FF=69.4%, J_{sc} = 17.4 mA/cm^2). While the film was casted on the hot substrate (HS) of 100 ℃without SV atmosphere, the evaporation process of the solvent was shortened [71,72]. As a result, the large-scale crystals of INPIC-4F were inhibited, thus the value of root-mean-square (RMS) surface roughness was reduced from 20 nm to 2.8 nm as shown in Figure 6c-h. The optimized morphology is beneficial to exciton dissociation (increased from 94.7% to 97.4%) and charge carrier collection

(increased from 80.1% to 84.8%). Moreover, the π-π stacking of INPIC-4F was also enhanced. As shown in Figure 6i, the diffraction peak at 1.85 Å-1 represents π-π stacking of INPIC-4F molecules. When cast on a HS with 100 ℃, the position of diffraction peak at 1.85 Å-1 moved to a higher qz. Furthermore, the absorption intensity of INPIC-4F increased as well (Figure 6j). All of these imply the tighter stacking and enhanced π-π packing of INPIC-4F, which is benefit for charge carrier transport. As a result, the electron and hole mobility increased from 8.7×10^{-5} cm^2 V^{-1} s^{-1} and 4.8×10^{-4} cm^2 V^{-1} s^{-1} to 6.6×10^{-4} cm^2 V^{-1} s^{-1} and 6.1×10-4 cm^2 V^{-1} s^{-1}, respectively. Consequently, the FF increased to 73.2% and J_{sc} increased to 21.8 mA/cm^2, which boosted the PCE to 13.1%.

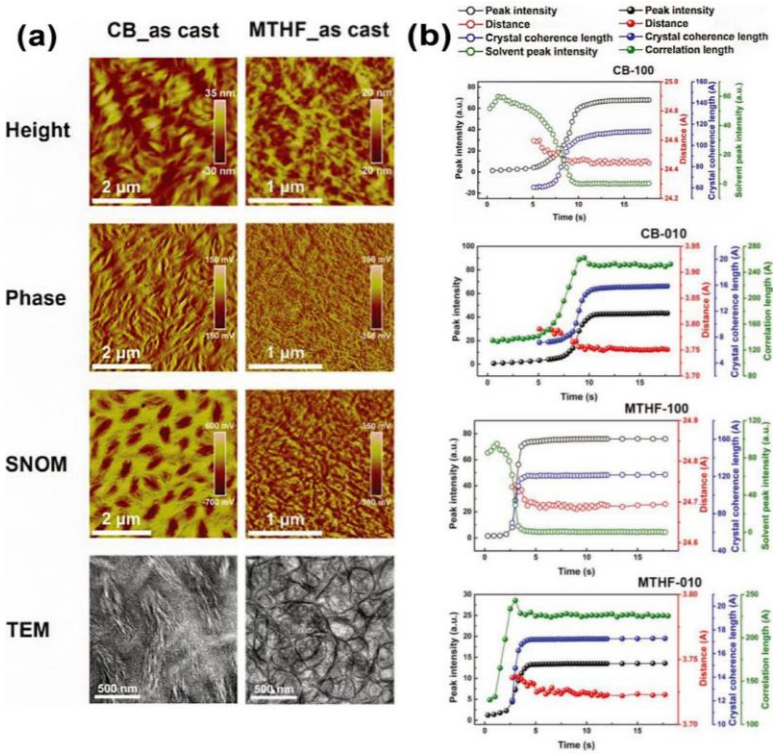

Figure 5: (a) Morphology of films treated with different solvents. Top to bottom are AFM height maps, phase diagrams, scattering-type scanning near-field optical microscopy SNOM and TEM. (b) (100) and (010) diffraction peak intensity of GIXD versus time [69].

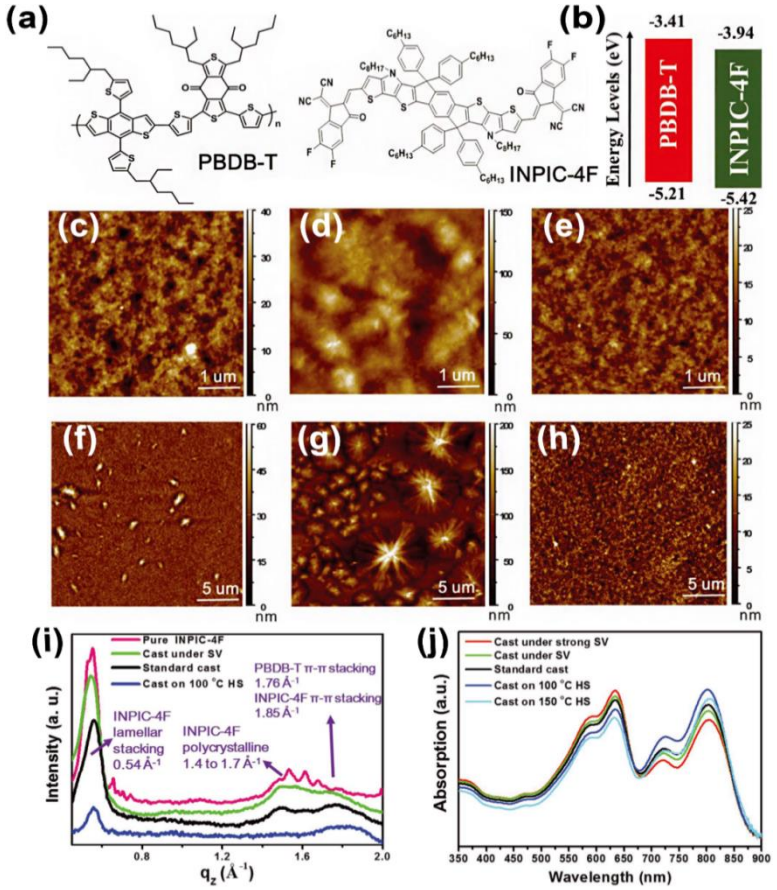

Figure 6: (a) molecular structure and (b) energy level diagram of PBDB-T and INPIC-4F. (c-h) AFM images of PBDB-T/INPIC-4F film surfaces at different magnifications: (c)(f) spin-coating, (d)(g) spin-coating in evaporation atmosphere, (e)(h) spin coating on a thermal substrate under 100 ℃. (i) GIWAXS diffraction intensity image of pure INPIC-4F film, PBDB-T/INPIC-4F film casted with room temperature in an SV atmosphere, in standard case, and on HS with 100 ℃. (j) absorption spectra of PBDB-T/INPIC-4F films prepared under different conditions [70].

The Film-Forming Kinetics Affect the Molecular Orientation of Donor and Acceptor

Conjugated molecules are highly anisotropic, and the strong electronic coupling is only expected for molecules oriented with

their π systems parallel to each other, which directly leads to the corresponding anisotropy of carrier mobility. Take P3HT for instance, the carrier mobility along the π-π stacking direction is approximately 10^{-2} cm^2 V^{-1} s^{-1}, but the one is lower along the alkyl side chain, which is only 10^{-4} cm^2 V^{-1} s^{-1}. As well known, conjugated molecule shows three different orientations in the film, i.e., edge-on (alkyl side chains are perpendicular to the substrate), face-on (π planes are parallel to the substrate) and flat-on orientation (the rigid backbones are perpendicular to the substrate) (Figure 7) [71]. According to the anisotropic carrier mobility, it can be deduced that the carrier transport along the direction perpendicular to the substrate is the lowest when the molecules adopt edge-on orientation. Unfortunately, conjugated molecule tends to adopt edge-on orientation because it is its thermodynamic stable state.

As we mentioned above, the longer film-forming process is, the easier is the formation of thermodynamic stable state. Hence, the edge-on orientation would be suppressed through shortening the film-forming duration [72]. Ryu et al. [73] studied the relationship between molecular orientation and film-forming methods. The results show that when the film was casted through drop casting, P3HT in film adopt edge-on orientation due to the long film-forming duration (about 30 min). While, the film-forming duration decreased to less than 20 secs when using spin-coating. As a result, P3HT was frozen in the sub-stable face-on orientation due to the insufficient organized time. Similarly, regulating the spin speed could modify the molecular orientation as well. DeLongchamp et al. [74] pointed that P3HT film casted with faster spin speed (2000 rpm) prefers face-on orientation compared to the one casted with slower spin speed (250 rpm). Consequently, the carrier mobility measured through effect transistors (FET) increased from of 1×10^{-3} cm^2 V^{-1} s^{-1} to 6×10^{-3} cm^2 V^{-1} s^{-1}.

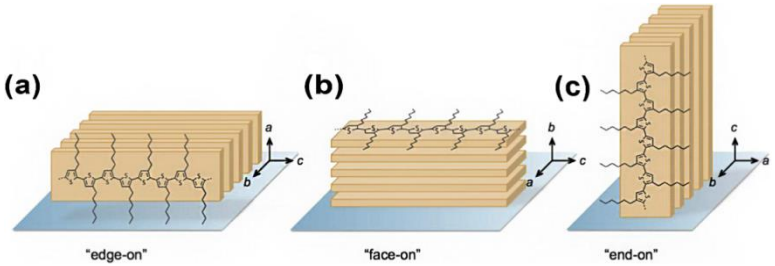

Figure 7: Three crystallographic orientations of polymer molecules [71].

The solvent also determines the film-forming kinetics to a large extent apart from film-forming method. Take poly{[N,N'-bis(2-octyldodecyl)-naphthalene-1,4,5,8-bis(dicarboximide)-2,6-diyl]-alt-5,5'-(2,2'-bithiophene)}(P(NDI2OD-T2))/poly[4,8-bis(5-(2-ethylhexyl)thiophen-2-yl)benzo[1,2-b:4,5-B']dithiophene-alt-3-fluorothieno[3,4-b]thiophene-2-carboxylate] (PTB7-th) blends for example, P(NDI2OD-T2) and PTB7-th adopted edge-on and face-on orientation respectively when using CN as solvent [75]. While if CN was substituted by solvents with relatively low b.p., such as o-dichlorobenzene (oDCB) and CB, the transition of P(NDI2OD-T2) orientation from edge-on to face-on in the PTB7-th/P(NDI2OD-T2) blends would occur, which was illustrated in Figure 8a and b. Therefore, the electron mobility increased from 1.01×10^{-5} cm^2 V^{-1} s^{-1} to 6.20×10^{-5} cm^2 V^{-1} s^{-1} and the PCE increased from 0.53% to 3.52% (Table 2). The orientation of Ph-DTDPo-TE:PBDB-T blend film changed from edge-on to face-on, the exciton dissociation probability increased from 93% to 96.3% [76]. The optimization is attributed the consistent molecular orientation of donor and acceptor molecules induces strong built-in electric field, which is benefit for the exciton dissociation.

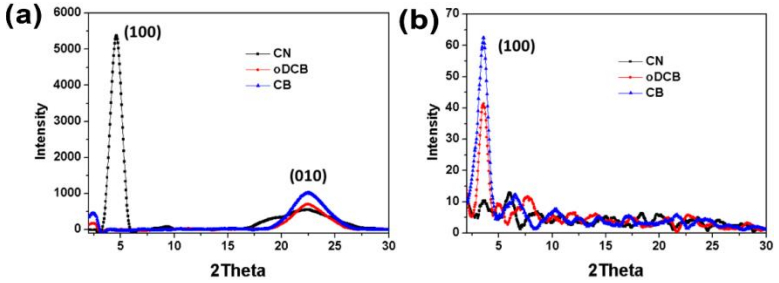

Figure 8: (a) Out-of-plane and (b) in-plane GIXD diffraction intensity for PTB7-th: P(NDI2OD-T2)=1:1 dry BHJ film cast from CN, o-DCB and CB [75].

Table 2: Device performance of different solvent treatment.

Solvent	μ_h (10^{-5} cm^2/(V s))	μ_e (10^{-5} cm^2/(V s))	PCE(%)
CN	0.62 ± 0.10	1.01 ± 0.16	0.53 ± 0.07
oDCB	3.90 ± 0.36	2.58 ± 0.26	2.73 ± 0.13
CB	8.40 ± 0.69	6.20 ± 1.51	3.52 ± 0.11

Combining the solvent engineering with spin speed is an effective strategy to regulate the film-forming kinetics. Kitchen et al. [77] combined spin speed with solvent to regulate the orientation of P3HT in P3HT/PCBM blends. It shows that when oDCB (b.p. 131°C), was selected as solvent and the film was casted through high spin speed, P3HT tended to adopt edge-on orientation. On the contrary, choosing chloroform (CF, b.p. 61 °C) as solvent and high spin speed could promote P3HT to adopt face-on orientation as shown in Figure 9. It is worth noting that corresponding to the transition from edge-on to face-on, the V_{oc} of solar cells increased from 0.26 V to 0.4 V. This is because the ionization energy of HOMO and the LUMO in the conjugated polymer are determined by the intrinsic surface dipoles, i.e., the HOMO level of P3HT with edge-on orientation is higher than the one with face-on orientation. Hence, the transition of molecular orientation from edge-on to face-on of P3HT leads to an increased gap between the HOMO of P3HT and the LUMO of PCBM, thus boosting the value of V_{oc}.

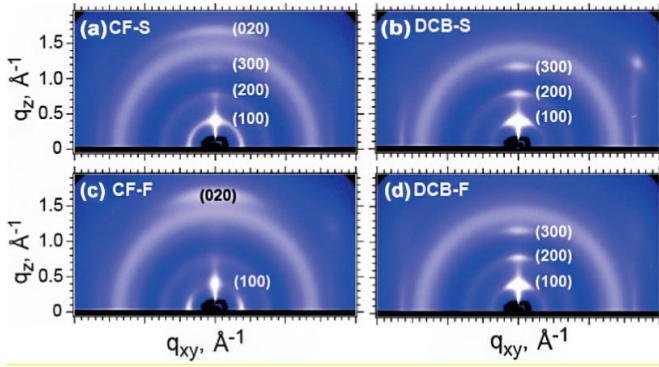

Figure 9: GIWAXS diffraction patterns of P3HT/PCBM films prepared under 4 different conditions [77].

The Film-Forming Kinetics Affect the Domain Sizes of the Blend Film

After the generation of excitons in BHJ solar cells, excitons would diffuse to the interface, then separate into free carriers [78]. The diffusion length of excitons in organic semiconductor materials is usually 5~10 nm [23,24,79]. If the domain sizes are too large, a large number of excitons cannot reach the D/A to dissociate and recombine to ground state as illustrates in Figure 10A. Hence, a small domain size is required for exciton dissociation. However, too small phase domain would induce the recombination between electrons and holes due to Coulomb's gravity during the charge transport. Therefore, the domain size should satisfy both the requirements of exciton dissociation and charge transport simultaneously.

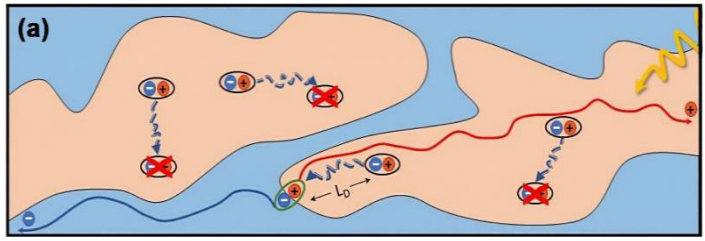

Figure 10: (a) Schematic illustration of exciton dissociation and carrier transport in large phase domains [80].

During the film-forming process, the duration of coarsening usually determines domain size. Kim et al. [81] studied the relationship between film-forming kinetics and domain size of poly{2,5-di(2-thienyl)thiophene-alt-6,7-difluoro-2,3-bis (3,4-bis-(octyloxy)phenyl)qunoxaline)}(PDFQx3T)/P(NDI2OD-T2)) blends. They employed solvents with different b.p., including CF, CB, oDCB and p-xylene (XY), and got domain size of 27 nm, 126 nm, 170 nm and 320 nm, respectively. The results indicate the solvent with low b.p. accelerates the film-forming process, which shorten the coarsening of phase separation. Compared with the large domain size (320 nm), the domain size of 27 nm is optimal for exciton quenching efficiency, which increased from 77.6% to 87.5%. Consequently, J_{sc} increased from 7.91 mA cm-2 to 10.58 mA cm^{-2}, thus boosting PCE from 3.83% to 5.11%.

Adjusting the composition of additives is also an effective strategy to controlling the domain size. Ma et al. [82] studied the relationship between the composition of additives and domain size. In FTAZ:ITIC-Th blends, ODT could promote the nucleation of donor and acceptor, while DIO could prolong the crystal growth process during film-forming stage. It shows that when the ratio of ODT to DIO is 0:0.5%, the phase domain size is 71 nm and the phase purity is 0.66; when the corresponding ratio is 0.375%:0.125%, the phase domain size reduced to 14 nm and the phase purity increased to 0.79. They ascribed the optimized morphology and PCE to the change of the film-forming kinetics (Figure 11bc): If only DIO exists, the film-forming duration would be extended excessively due to its high b.p. and induce a large domain size. When adding ODT as the other additive, the volatile ODT could induce the nucleation within 100 s, while DIO still existed in the film for a longer period (>100 s), which could further promote the crystal growth. Due to the compromise between nucleation and crystal growth, the domain size was decreased, while the domain purity was increased. The optimized morphology is benefit for exciton dissociation and charge transport, leading PCE increased from 9.04% to 10.93%.

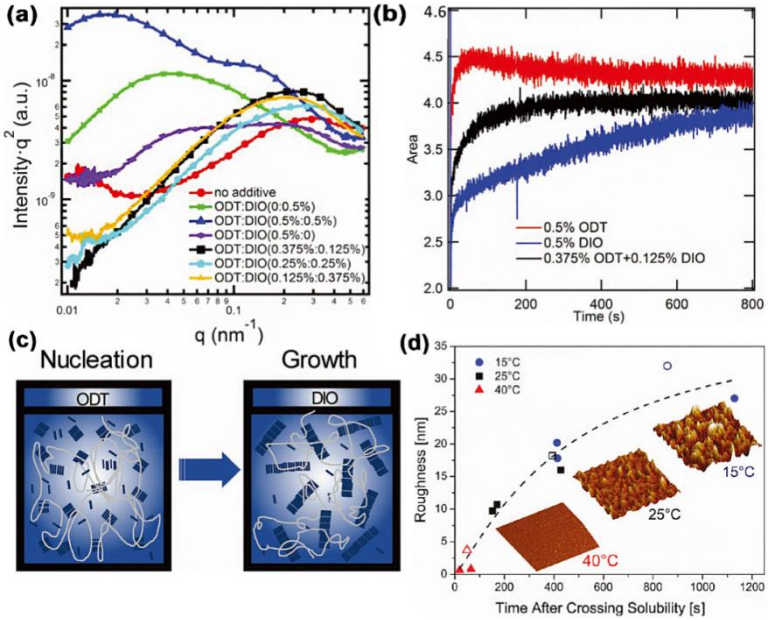

Figure 11:(a) Reduced RSoXS data of films with different composition. (b) In situ GIWAXS data of the (010) diffraction peak of FTAZ/ITIC-Th(1:1.5, w/w) films processed from additives of different composition. (c) Schematic of the effect of ODT and DIO additives on the crystallinity of the active layer [82]. (d) The evolution of roughness of films deposited under various temperatures (Solid is P3HT/PCBM, hollow is pure P3HT) [60].

As we mentioned above, too small domain size is not benefit for the charge transport, and extending the film-forming duration is an effective method to enlarge the domain size [83]. Barrena et al. [60] decreased the flow rate of the dry gas (N2) and the film-forming temperature (Figure 11d) to extend the film-forming duration of P3HT/PCBM blend. When the flow rate was decreased to 0.5 m/s, turning the film-forming temperature from 40 °C to 15 °C, the film-forming duration would be prolonged from less than 100 s to around 1100 s. The prolonged duration provides enough time for phase coarsening, resulting in larger domain size, which can be deduced by the increased a large root mean square (RMS) from less than2.5 nm to around 25 nm. The enlarged domain size could suppress the biomolecular recombination, increasing J_{sc} from 3.2 mA/cm^2 to 7.2 mA/cm^2. Similarly, adding high b.p. additive could increase the domain

size as well. Manley et al. [84] extended the film-forming duration of PTB7 film from about 9 s to 5580 s by adding DIO, and the coherence lengths (CLs) increased from 1.99 to 2.36 nm, whose effect of optimizing PCE has been verified [85].

The Film-Forming Kinetics Affect the Phase Separation Structure of the Blend Film

In order to ensure carriers transport to the corresponding electrodes effectively, the donor and acceptor should form continuous phases, respectively, i.e., bi-continuous lateral phase separation or interpenetrating network [86]. If the donor and/or acceptor form isolated island-like phase separation structure, the bimolecular recombination of carrier would be serious, which cause low FF and J_{sc} of device. In addition to the lateral bi-continuous structure, the vertical phase separation structure, referring to the distribution of donor and acceptor in the perpendicular direction to the substrate, also plays an important role in the charge transport and collection. Recent studies show an ideal vertical phase separation structure should be described as donors enrich near the anode and acceptors enrich near the cathode, which is expected to improve the charge transport and collection efficiency [87,88].

Promoting the aggregation of fullerene in polymer/fullerene blends is benefit for the formation of interpenetrating network. Heeger et al. prolonged the film-forming time of the [2,6-(4,4-bis(2-ethylhexyl)-4H-cyclopenta[2,1-b;3,4-b']-dithiophene)-alt-4,7-(2,1,3-benzothiadiazole)] (PCPDTBT)/$PC_{71}BM$ blends by adding DIO as additive. Due to the high b.p. and selective solubility to $PC_{71}BM$ of DIO, PCPDTBT precipitates in advance after the evaporation of main solvent, while $PC_{71}BM$ still dissolved in DIO. Consequently, the crystallization process of PCPDTBT and $PC_{71}BM$ occurred in different stages. Without the disturb between donor and acceptor and the prolonged film-forming process, it is easy for PCPDTBT and $PC_{71}BM$ to self-organize into continuous pathways [89]. In order to confirm the formation of continuous structure, the authors removed the $PC_{71}BM$ in the blend film as shown in Figure 12. It is obvious that the residual PCPDTBT formed island-like phase separation

structure without additive. While after adding DIO, continuous pathways formed due to the formation of PCPDTBT fibers, and the aggregated fullerene filled in the space between polymer fibers, thus a bi-continuous structure was formed. The optimized phase separation structure was beneficial for the device performance, resulting in the increase of J_{sc} from 11.74mA/cm^2 to 15.73mA/cm^2 and the PCE from 3.35% to 5.12%.

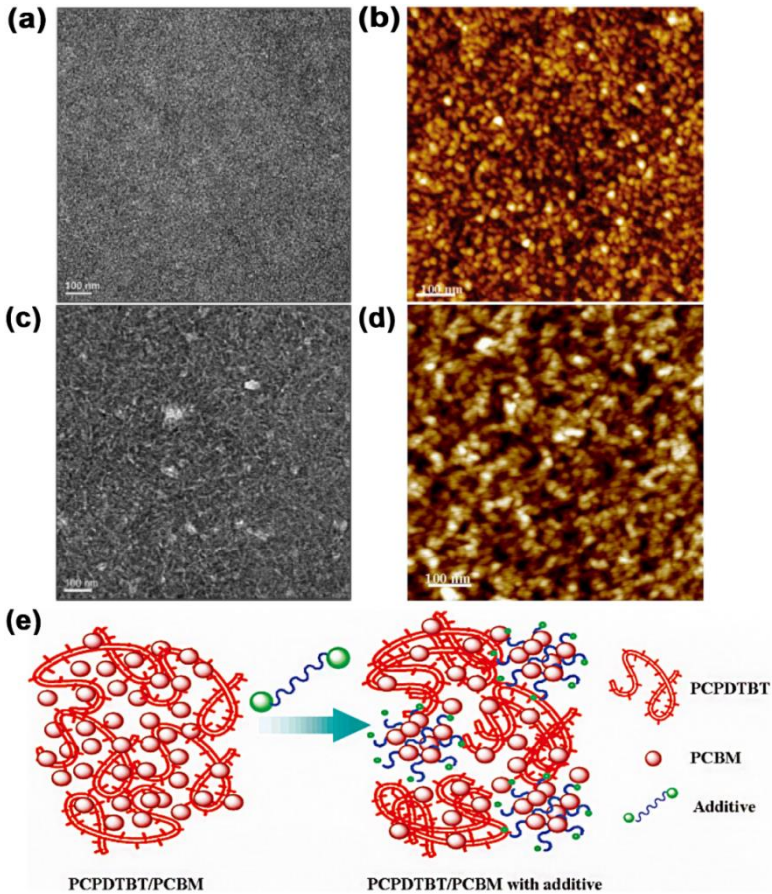

Figure 12: TEM image of PCPDTBT/$PC_{71}BM$ film (a) without and (c) with the addition of the 1,8-diiodooctane. AFM diagram of PCPDTBT network structure after the removal of $PC_{71}BM$ film treated (b) without and (d) with 1,8-diiodooctane. (e) Schematic illumination of the action of the 1,8-diiodooctane in the self-assembly of bulk heterojunction blend materials [89].

The vertical phase separation structure could be optimized by regulating film-forming process as well. Sun et al. [90] prolonged the film-forming process of P3HT/PCBM blend by adding tetralin as additive. As the X-ray photoelectron spectroscopy (XPS) (Figure 13ab) shows that the quality ratio of PCBM to P3HT (mPCBM:mP3HT) near the film surface increased from 0.1 to 0.72 after adding CN. This variation was ascribed to the high solubility of PCBM and slow volatilization rate of CN compared to main solvent. At the late stage of film-forming process, parts of PCBM dissolved in the residual CN. As evaporation of CN, PCBM would migrate from the inside to the surface of the film drove by the directed diffusion of CN. This kind of vertical phase separation is benefit for charge transport and collection of devices with normal structure. Thus, the PCE is 1.5 times higher than the device fabricated from the solution without CN.

Combining the film-forming kinetics and surface tension is also an effective way to optimize the vertical phase separation. Liang et al. [42] added 1,2,4-triclorobenzene (TCB) to the CB solution of the P3HT/(5Z,5'Z)-5,5'-((7,7'-(4,4,9,9-tetraoctyl-4,9-dihydro-s-indaceno[1,2-b:5,6-b']dithiophene-2,7-diyl)bis(benzo[c][1,2,5]thiadiazole7,4diyl))bis(methanylylidene))bis(3-ethyl-2-thioxothiazolidin-4-one) (O-IDTBR) blends to improve its vertical phase separation. After adding TCB, the content of P3HT near the top surface increased from 89% to 96%, while the content of P3HT near the bottom of the film decreased from 50% to 42% according to depth-dependent absorption spectra as shown in Figure 13c. These variations can be interpreted by the differences in characters between CB and TCB, especially their b.p. and the solubility of solutes in them. Due to the lower surface tension of P3HT compared with PCBM (γP3HT = 21.1 mN/m < γO-IDTBR = 28.1 mN/m), P3HT in the P3HT/PCBM blends is inclined to move to the top surface to decrease the Gibbs free energy during the film-forming process. When using CB as solvent, the film-forming process was ~50 s, a large number of P3HT have no enough time to migrate. Therefore, the vertical phase separation was not thorough. While after adding TCB, TCB has higher b.p. than the main solvent CB, which prolonged the film-forming process to about 210 s.

Meanwhile, the solubility of P3HT and O-IDTBR in TCB is higher the one in CB. Hence, after the volatilization of CB, a mass of P3HT and O-IDTBR still dissolved in TCB. As TCB evaporates, P3HT has enough time to migrate, leading to more P3HT distributed on the top surface of film. The optimized morphology suppressed the bimolecular recombination (the exponential factor α increased from 0.96 to 0.98), boosting the PCE from 4.45% to 7.18% in an inverted device structure. Similar phenomenon was observed in polymer/fullerene blends as well. Yang et al. used DCB as main solvent and 1,8-octanedithiol (OT) as additive in P3HT/PCBM blend. The addition of OT increased the content of P3HT at film surface and decreased the content of PCBM at film bottom as shown in Figure 13d, which increased PCE by 10 times from the initial ~0.29%. All the examples demonstrate that changing the film-forming kinetic to optimize the lateral and vertical phase separation structure of the active layer is an effective method to improve the device performance of OCSs.

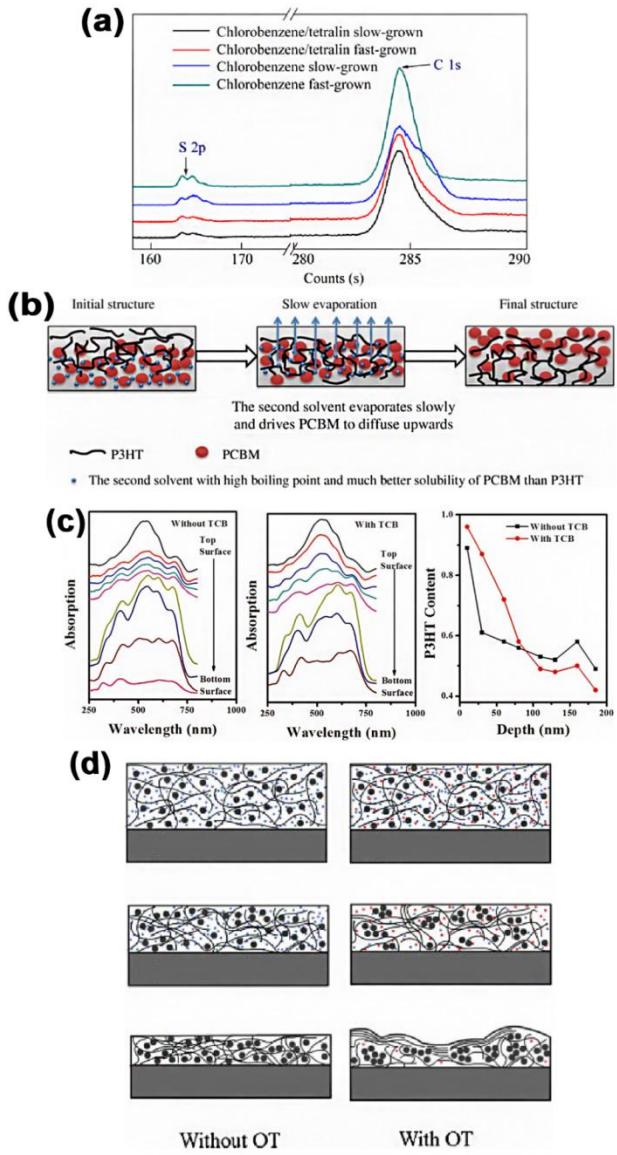

Figure 13: (a) XPS spectrum. (b) Schematic of the role of solvent evaporation rate [90]. (c) Film-depth-dependent light absorption spectra of P3HT:O-IDTBR blend film prepared under different conditions. Top and bottom surfaces represent P3HT:O-IDTBR/MoO3 and ZnO/P3HT:O-IDTBR interfaces, respectively. (d) Schematic diagram of morphology evolution in films treated with two types of solvent [91].

Summary and Perspectives

The photovoltaic performance of OSCs is closely related to the BHJ morphology of the active layer, because the crystallinity, molecular orientation, domain size and phase separation structure have profound influence on the exciton dissociation, charge transport and collection. As we know the morphology of BHJ is kinetically frozen structure. Hence, regulating the duration of film-forming process, including solvent engineering and adjusting the substrate temperature, is an effective way to optimize the morphology of the active layer. Film-forming process contains solvent evaporation and solutes solidification, thus regulating the b.p. of solvents and spin speed and so on is effective to optimize the morphology. Specifically, prolonging the film-forming process could extend the duration of molecular diffusion, which is benefit for the crystallization and phase separation, thus high crystallinity and large domain size with high phase purity were achieved. Moreover, the shortening the film-forming process could promote the molecules to stay at metastable state, in which the molecules tend to adopt face-on orientation. Furthermore, the selective solubility and high b.p. of additive could also regulate the sequence of solidification between donor and acceptor, promoting the formation of interpenetrating networks with optimized lateral phase separation. Overall, the examples demonstrated herein offer a rational guide to understand the foundation of film-forming kinetics on optimizing the BHJ morphology of active layer.

Presently, OSCs based on polymer/nonfullerene blends dominate the development of OSCs. The morphology optimization of the nonfullerene-based blend films empirically follows the various treatments originally developed in polymer/fullerene blends. Considering the different properties between nonfullerene and fullerene derivatives, such as solubility in solvent, miscibility between donor and acceptor and molecular diffusivity, morphology optimization should take comprehensive attention to the molecular properties of the active layer, and rational morphology control treatments should be developed toward the combination of improved efficiency and increased stability. Additionally, solvent engineering is highly

meet the requirement for practical application of OSCs, such as the fabrication of large-area and flexible OSCs. Hence, thorough comprehension about film-forming kinetics in non-halogenated additives during large-area film-forming process, such as doctor blading, roll-to-roll and ink-jet printing, should be taken into account to fabricate OSCs for their future application

References

1. Servaites JD, Ratner MA, Marks TJ. Organic solar cells: A new look at traditional models. Energ Environ. Sci. 2011; 4: 4410-4422.
2. Service RF. Solar energy. Outlook brightens for plastic solar cells. Science. 2011; 332: 293.
3. Dou L, You J, Hong Z, Xu Z, Li G, et al. 25th anniversary article: a decade of organic/polymeric photovoltaic research. Adv. Mater. 2013; 25: 6642-71.
4. Krebs FC, Espinosa N, Hosel M, Sondergaard RR, Jorgensen M. 25th anniversary article: Rise to power--OPV-based solar parks. Adv. Mater. 2014; 26: 29-38.
5. Liu Q, Jiang Y, Jin K, Qin J, Xu J, et al. 18% Efficiency organic solar cells. Sci. Bull. 2020; 65: 272-275.
6. Song J, Zhu L, Li C, Xu J, Wu H, et al. High-efficiency organic solar cells with low voltage loss induced by solvent additive strategy. Matter. 2021; 4: 2542-2552.
7. Meng H, Liao C, Deng M, Xu X, Yu L, et al. 18.77 % Efficiency Organic Solar Cells Promoted by Aqueous Solution Processed Cobalt(II) Acetate Hole Transporting Layer. Angew. Chem, Int. Ed. Engl. 2021; 133: 22728 – 22735.
8. Liu L, Chen S, Qu Y, Gao X, Han L, et al. Nanographene-Osmapentalyne Complexes as a Cathode Interlayer in Organic Solar Cells Enhance Efficiency over 18. Adv. Mater. 2021; 33: 2101279.
9. Liu G, Xia R, Huang Q, Zhang K, Hu Z, et al. Tandem Organic Solar Cells with 18.7% Efficiency Enabled by Suppressing the Charge Recombination in Front Sub-Cell. Adv. Funct. Mater. 2021; 31: 2103283.
10. Li C, Zhou J, Song J, Xu J, Zhang H, et al. Non-fullerene acceptors with branched side chains and improved molecular

packing to exceed 18% efficiency in organic solar cells. Nat. Energy. 2021; 6: 605–613.
11. Jin K, Xiao Z, Ding L. 18.69% PCE from organic solar cells. J. Semicond. 2021; 42.
12. Guo C, Li D, Wang L, Du B, Liu ZX, et al. Cold-Aging and Solvent Vapor Mediated Aggregation Control toward 18% Efficiency Binary Organic Solar Cells. Adv. Energy Mater. 2021; 2102000.
13. Zhang T, An C, Bi P, Lv Q, Qin J, et al. A Thiadiazole-Based Conjugated Polymer with Ultradeep HOMO Level and Strong Electroluminescence Enables 18.6% Efficiency in Organic Solar Cell. Adv. Energy Mater. 2021; 11: 2101705.
14. Liu F, Zhou L, Liu W, Zhou Z, Yue Q, et al. Organic Solar Cells with 18% Efficiency Enabled by an Alloy Acceptor: A Two-in-One Strategy. Adv. Mater. 2021; 33: 2100830.
15. Lin Y, Magomedov A, Firdaus Y, Kaltsas D, El-Labban A, et al. 18.4 % Organic Solar Cells Using a High Ionization Energy Self-Assembled Monolayer as Hole-Extraction Interlayer. ChemSusChem. 2021; 14: 3569-3578.
16. Li Y, Cai Y, Xie Y, Song J, Wu H, et al. A facile strategy for third-component selection in non-fullerene acceptor-based ternary organic solar cells. Energ Environ. Sci. 2021; 14: 5009-5016.
17. Cui Y, Xu Y, Yao H, Bi P, Hong L, et al. Single-Junction Organic Photovoltaic Cell with 19% Efficiency. Adv. Mater. 2021; 2102420.
18. Chen X, Wang D, Wang Z, Li Y, Zhu H, et al. 18.02% Efficiency ternary organic solar cells with a small-molecular donor third component. Chem. Eng. J. 2021; 424: 130397.
19. Cai Y, Li Y, Wang R, Wu H, Chen Z, et al. A Well-Mixed Phase Formed by Two Compatible Non-Fullerene Acceptors Enables Ternary Organic Solar Cells with Efficiency over 18.6. Adv. Mater. 2021; 33: 2101733.
20. Mazzio KA, Luscombe CK. The future of organic photovoltaics. Chem Soc Rev. 2015; 44: 78-90.
21. Hood SN, Kassal I. Entropy and Disorder Enable Charge Separation in Organic Solar Cells. J. Phys. Chem. Lett. 2016; 7: 4495-4500.
22. Scharber MC, Sariciftci NS. Efficiency of bulk-heterojunction organic solar cells. Prog. Polym. Sci. 2013;

38: 1929-1940.
23. Gulen D. Determination of the Exciton Diffusion Length by Surface Quenching Experiments. J. Lumin. 1988; 42: 191-195.
24. Hong NH, Sakai J, Huong NT, Poirot N, Ruyter A. Role of defects in tuning ferromagnetism in diluted magnetic oxide thin films. Phys. Rev. B 2005; 72: 045336.
25. Zhang R, Yang H, Zhou K, Zhang J, Liu J, et al. Optimized domain size and enlarged D/A interface by tuning intermolecular interaction in all-polymer ternary solar cells. J. Poly. Sci. 2016; 54: 1811-1819.
26. Chen S, Zhang L, Ma C, Meng D, Zhang J, et al. Alkyl Chain Regiochemistry of Benzotriazole-Based Donor Polymers Influencing Morphology and Performances of Non-Fullerene Organic Solar Cells. Adv. Energy Mater. 2018; 8: 1702427.
27. Zhou K, Zhao Q, Zhang R, Cao X, Yu X, et al. Decreased domain size of p-DTS(FBTTh2)2/P(NDI2OD-T2) blend films due to their different solution aggregation behavior at different temperatures. Phys. Chem. Chem. Phys. 2017; 19: 32373-32380.
28. Xiao B, Du M, Wang X, Xiao Z, Li G, et al. Effects of Oxygen Atoms Introduced at Different Positions of Non-Fullerene Acceptors in the Performance of Organic Solar Cells with Poly(3-hexylthiophene). ACS Appl. Mater. Inter. 2020; 12: 1094-1102.
29. Zhou K, Wu Y, Liu Y, Zhou X, Zhang L, et al. Molecular Orientation of Polymer Acceptor Dominates Open-Circuit Voltage Losses in All-Polymer Solar Cells. Acs Energy Lett. 2019; 4: 1057-1064.
30. Rand BP, Cheyns D, Vasseur K, Giebink NC, Mothy S, et al. The Impact of Molecular Orientation on the Photovoltaic Properties of a Phthalocyanine/Fullerene Heterojunction. Adv. Funct. Mater. 2012; 22: 2987-2995.
31. Zhang Q, Xiao B, Du M, Li G, Tang A, et al. A2–A1–D–A1–A2 type non-fullerene acceptors based on methoxy substituted benzotriazole with three different end-capped groups for P3HT-based organic solar cells. J. Mater. Chem. C 2018; 6: 10902-10909.
32. Xiao B, Tang A, Zhang J, Mahmood A, Wei Z, et al.

Achievement of High Voc of 1.02 V for P3HT-Based Organic Solar Cell Using a Benzotriazole-Containing Non-Fullerene Acceptor. Adv. Energy Mater. 2017; 7: 1602269.
33. Qiu N, Yang X, Zhang H, Wan X, Li C, et al. Nonfullerene Small Molecular Acceptors with a Three-Dimensional (3D) Structure for Organic Solar Cells. Chem Mater. 2016; 28: 6770-6778.
34. Liang Q, Han J, Song C, Yu X, Smilgies DM, et al. Reducing the confinement of PBDB-T to ITIC to improve the crystallinity of PBDB-T/ITIC blends. J. Mater. Chem. A 2018; 6: 15610-15620.
35. Liu J, Zeng S, Zhang Z, Peng J, Liang Q. Optimizing the Phase-Separated Domain Size of the Active Layer via Sequential Crystallization in All-Polymer Solar Cells. J. Phys. Chem. Lett. 2020; 11: 2314-2321.
36. Xu X, Zhang G, Yu L, Li R, Peng Q. P3HT-Based Polymer Solar Cells with 8.25% Efficiency Enabled by a Matched Molecular Acceptor and Smart Green-Solvent Processing Technology. Adv. Mater. 2019; 31: 1906045.
37. Yang C, Yu R, Liu C, Li H, Zhang S, et al. Achieving over 10 % Efficiency in Poly(3-hexylthiophene)-based Organic Solar Cells via Solid Additives. ChemSusChem. 2021; 14: 3607–3613.
38. Liu F, Zhang JY, Zhou ZC, Zhang JQ, Wei ZX, et al. Poly(3-hexylthiophene)-based non-fullerene solar cells achieve high photovoltaic performance with small energy loss. J. Mater. Chem. A 2017; 5: 16573-16579.
39. Li S, Liu W, Shi M, Mai J, Lau TK, et al. A spirobifluorene and diketopyrrolopyrrole moieties based non-fullerene acceptor for efficient and thermally stable polymer solar cells with high open-circuit voltage. Energ Environ. Sci. 2016; 9: 604-610.
40. Holliday S, Ashraf RS, Wadsworth A, Baran D, Yousaf SA, et al. High-efficiency and air-stable P3HT-based polymer solar cells with a new non-fullerene acceptor. Nat. Commun. 2016; 7: 11585.
41. Liu J, Zeng S, Jing P, Zhao K, Liang Q. Investigating the effect of cosolvents on P3HT/O-IDTBR film-forming kinetics and film morphology. J. Energy Chem. 2020; 51: 333-341.

42. Liang Q, Jiao X, Yan Y, Xie Z, Lu G, et al. Separating Crystallization Process of P3HT and O-IDTBR to Construct Highly Crystalline Interpenetrating Network with Optimized Vertical Phase Separation. Adv. Funct. Mater. 2019; 29: 1807591.
43. Wang X, Sun Q, Gao J, Wang J, Xu C, et al. Recent Progress of Organic Photovoltaics with Efficiency over 17%. Energies. 2021; 14: 4200.
44. Liao KS, Yambem SD, Haldar A, Alley NJ, Curran SA. Designs and Architectures for the Next Generation of Organic Solar Cells. Energies. 2010; 3: 1212-1250.
45. Zhao Y, Yuan GX, Roche P, Leclerc M. A Calorimetric Study of the Phase-Transitions in Poly(3-Hexylthiophene). Polymer. 1995; 36: 2211-2214.
46. Dittmer JJ, Lazzaroni R, Leclere P, Moretti P, Granstrom M, et al. Crystal network formation in organic solar cells. Sol. Energ. Mat. Sol. C 2000; 61: 53-61.
47. Padinger F, Rittberger RS, Sariciftci NS. Effects of postproduction treatment on plastic solar cells. Adv. Funct. Mater. 2003; 13: 85-88.
48. Jenekhe SA, Yi SJ. Highly photoconductive nanocomposites of metallophthalocyanines and conjugated polymers. Adv. Mater. 2000; 12: 1274.
49. Ma W, Yang C, Gong X, Lee K, Heeger AJ. Thermally Stable, Efficient Polymer Solar Cells with Nanoscale Control of the Interpenetrating Network Morphology. Adv. Funct. Mater. 2005; 15: 1617-1622.
50. Lee H, Oh S, Song CE, Lee HK, Lee SK, et al. Stable P3HT: amorphous non-fullerene solar cells with a high open-circuit voltage of 1 V and efficiency of 4%. RSC Adv. 2019; 9: 20733-20741.
51. Jang M, Huh YI, Chang M. Effects of Solvent Vapor Annealing on Morphology and Charge Transport of Poly(3-hexylthiophene) (P3HT) Films Incorporated with Preformed P3HT Nanowires. Polymers. 2020; 12: 1188.
52. Li G, Shrotriya V, Huang J, Yao Y, Moriarty T, et al. High-efficiency solution processable polymer photovoltaic cells by self-organization of polymer blends. Nat. Mat. 2005; 4: 864-868.
53. Wu J, Yuan Y, Gao M, Wang Z, Jiang L. Preparation of

Single Crystals of Small Molecule Organic Semiconductor via Solvent Vapor Annealing. Acta. Chim. Sinica. 2015; 73: 23—28.
54. Vogelsang J, Brazard J, Adachi T, Bolinger JC, Barbara PF. Watching the annealing process one polymer chain at a time. Angew. Chem. Int. Ed. Engl. 2011; 50: 2257-2261.
55. Hammed W, Yahya R, Bola A, Mahmud H. Recent Approaches to Controlling the Nanoscale Morphology of Polymer-Based Bulk-Heterojunction Solar Cells. Energies. 2013; 6: 5847-5868.
56. Yang L, Zhang S, He C, Zhang J, Yao H, et al. New Wide Band Gap Donor for Efficient Fullerene-Free All-Small-Molecule Organic Solar Cells. J. Am. Chem. Soc. 2017; 139: 1958-1966.
57. Chang YM, Wang L. Efficient Poly(3-hexylthiophene)-Based Bulk Heterojunction Solar Cells Fabricated by an Annealing-Free Approach. J. Phys. Chem. C 2008; 112: 17716-17720.
58. Berson S, De Bettignies R, Bailly S, Guillerez S. Poly(3-hexylthiophene) Fibers for Photovoltaic Applications. Adv. Funct. Mater. 2007; 17: 1377-1384.
59. Buss F, Schmidt-Hansberg B, Sanyal M, Munuera C, Scharfer P, et al. Gaining Further Insight into the Solvent Additive-Driven Crystallization of Bulk-Heterojunction Solar Cells by in Situ X-ray Scattering and Optical Reflectometry. Macromolecules. 2016; 49: 4867-4874.
60. Schmidt-Hansberg B, Sanyal M, Klein MFG, Pfaff M, Schnabel N, et al. Moving through the Phase Diagram: Morphology Formation in Solution Cast Polymer-Fullerene Blend Films for Organic Solar Cells. Acs Nano. 2011; 5: 8579-8590.
61. Shin N, Richter LJ, Herzing AA, Kline RJ, DeLongchamp DM. Effect of Processing Additives on the Solidification of Blade-Coated Polymer/Fullerene Blend Films via In-Situ Structure Measurements. Adv. Energy Mater. 2013; 3: 938-948.
62. Turner ST, Pingel P, Steyrleuthner R, Crossland EJW, Ludwigs S, et al. Quantitative Analysis of Bulk Heterojunction Films Using Linear Absorption Spectroscopy and Solar Cell Performance. Adv. Funct. Mater. 2011; 21:

4640-4652.
63. Landi G, Barone C, Mauro C, De Sio A, Carapella G, et al. Probing Temperature-Dependent Recombination Kinetics in Polymer:Fullerene Solar Cells by Electric Noise Spectroscopy. Energies. 2017; 10: 1490.
64. Engmann S, Bokel FA, Ro HW, DeLongchamp DM, Richter LJ. Real-Time Photoluminescence Studies of Structure Evolution in Organic Solar Cells. Adv. Energy Mater. 2016; 6: 1502011.
65. Sim M, Shin J, Shim C, Kim M, Jo SB, et al. Dependence of Exciton Diffusion Length on Crystalline Order in Conjugated Polymers. J. Phys. Chem. C. 2014; 118: 760-766.
66. Burkhard GF, Hoke ET, Scully SR, McGehee MD. Incomplete exciton harvesting from fullerenes in bulk heterojunction solar cells. Nano Lett. 2009; 9: 4037-4041.
67. Richter LJ, DeLongchamp DM, Bokel FA, Engmann S, Chou KW, et al. In Situ Morphology Studies of the Mechanism for Solution Additive Effects on the Formation of Bulk Heterojunction Films. Adv. Energy Mater. 2015; 5: 1400975.
68. McDowell C, Abdelsamie M, Zhao K, Smilgies DM, Bazan GC, et al. Synergistic Impact of Solvent and Polymer Additives on the Film Formation of Small Molecule Blend Films for Bulk Heterojunction Solar Cells. Adv. Energy Mater. 2015; 5: 1501121.
69. Zhu L, Zhong W, Qiu C, Lyu B, Zhou Z, et al. Aggregation-Induced Multilength Scaled Morphology Enabling 11.76% Efficiency in All-Polymer Solar Cells Using Printing Fabrication. Adv. Mater. 2019; 31: 1902899.
70. Li W, Chen M, Zhang Z, Cai J, Zhang H, et al. Retarding the Crystallization of a Nonfullerene Electron Acceptor for High-Performance Polymer Solar Cells. Adv. Funct. Mater. 2018; 29: 1807662.
71. Osaka I, Takimiya K. Backbone orientation in semiconducting polymers. Polymer. 2015; 59: 1-15.
72. Rogers JT, Schmidt K, Toney MF, Bazan GC, Kramer EJ. Time-resolved structural evolution of additive-processed bulk heterojunction solar cells. J. Am. Chem. Soc. 2012; 134: 2884-2887.

73. Spano FC. Modeling disorder in polymer aggregates: the optical spectroscopy of regioregular poly(3-hexylthiophene) thin films. J. Chem. Phys. 2005; 122: 234701.
74. DeLongchamp DM, Vogel BM, Jung Y, Gurau MC, Richter CA, et al. Variations in semiconducting polymer microstructure and hole mobility with spin-coating speed. Chem. Mater. 2005; 17: 5610-5612.
75. Zhou K, Zhang R, Liu J, Li M, Yu X, et al. Donor/Acceptor Molecular Orientation-Dependent Photovoltaic Performance in All-Polymer Solar Cells. ACS Appl. Mater. Inter. 2015; 7: 25352-25361.
76. Li M, Zhou Y, Yang L, Shen S, Liu Y, et al. Regulating molecular orientations of dipyran-based nonfullerene acceptors through side-chain engineering at the π-bridge. J. Mater. Chem. A 2020; 8: 22416-22422.
77. Kitchen B, Awartani O, Kline RJ, McAfee T, Ade H, et al. Tuning Open-Circuit Voltage in Organic Solar Cells with Molecular Orientation. ACS Appl. Mater. Inter. 2015; 7: 13208-13216.
78. Luhman WA, Holmes RJ. Investigation of Energy Transfer in Organic Photovoltaic Cells and Impact on Exciton Diffusion Length Measurements. Adv. Funct. Mater. 2011; 21: 764-771.
79. Han J, Liang Q, Qu Y, Liu J, Han Y. Morphology Control of Non-fullerene Blend Systems Based on Perylene. Acta Phys.-Chimi. Sin. 2018; 34: 391-406.
80. Gaspar H, Figueira F, Pereira L, Mendes A, Viana JC, et al. Recent Developments in the Optimization of the Bulk Heterojunction Morphology of Polymer: Fullerene Solar Cells. Materials. 2018; 11: 2560.
81. Lee C, Li Y, Lee W, Lee Y, Choi J, et al. Correlation between Phase-Separated Domain Sizes of Active Layer and Photovoltaic Performances in All-Polymer Solar Cells. Macromolecules. 2016; 49: 5051-5058.
82. Chen J, Bi Z, Xu X, Zhang Q, Yang S, et al. Fine Optimization of Morphology Evolution Kinetics with Binary Additives for Efficient Non-Fullerene Organic Solar Cells. Adv. Sci. 2019; 6: 1801560.
83. Ruderer MA, Guo S, Meier R, Chiang HY, Körstgens V, et al. Solvent-Induced Morphology in Polymer-Based Systems

for Organic Photovoltaics. Adv. Funct. Mater. 2011; 21: 3382-3391.
84. Manley EF, Strzalka J, Fauvell TJ, Jackson NE, Leonardi MJ, et al. In Situ GIWAXS Analysis of Solvent and Additive Effects on PTB7 Thin Film Microstructure Evolution during Spin Coating. Adv. Mater. 2017; 29: 1703933.
85. Chen H, Tang H, Hu D, Xiao Y, Fu J, et al. Design of All-Small-Molecule Organic Solar Cells Approaching 14% Efficiency via Isometric Terminal Alkyl Chain Engineering. Energies. 2021; 14: 2505.
86. Lee H, Park C, Sin DH, Park JH, Cho K. Recent Advances in Morphology Optimization for Organic Photovoltaics. Adv. Mater. 2018; 30: 1800453.
87. Ayzner AL, Tassone CJ, Tolbert SH, Schwartz BJ. Reappraising the Need for Bulk Heterojunctions in Polymer-Fullerene Photovoltaics: The Role of Carrier Transport in All-Solution-Processed P3HT/PCBM Bilayer Solar Cells. J. Phys. Chem. C 2009; 113: 20050-20060.
88. de Villers BT, Tassone CJ, Tolbert SH, Schwartz BJ. Improving the Reproducibility of P3HT:PCBM Solar Cells by Controlling the PCBM/Cathode Interface. J. Phys. Chem. C 2009; 113: 18978-18982.
89. Lee JK, Ma WL, Brabec CJ, Yuen J, Moon JS, et al. Processing additives for improved efficiency from bulk heterojunction solar cells. J. Am. Chem. Soc.2008; 130: 3619-3623.
90. Sun Y, Liu J, Ding Y, Han Y. Controlling the surface composition of PCBM in P3HT/PCBM blend films by using mixed solvents with different evaporation rates. Chinese J. Poly. Sci. 2013; 31: 1029-1037.
91. Yao Y, Hou J, Xu Z, Li G, Yang Y. Effects of Solvent Mixtures on the Nanoscale Phase Separation in Polymer Solar Cells. Adv. Funct. Mater. 2008; 18: 1783-1789.